

Supporting Information

# Coprecipitation-Gel Synthesis and Degradation Mechanism of Octahedral $\text{Li}_{1.2}\text{Mn}_{0.54}\text{Ni}_{0.13}\text{Co}_{0.13}\text{O}_2$ as High-Performance Cathode Materials for Lithium-ion Batteries

*Wenxiang He,<sup>†,§</sup> Jianguo Liu,<sup>\*,†,‡</sup> Wei Sun,<sup>\*,§</sup> Wuwei Yan,<sup>‡</sup> Liang Zhou,<sup>‡</sup> Congping Wu,<sup>‡</sup>  
Junsheng Wang,<sup>§</sup> Xinliang Yu,<sup>§</sup> Haimin Zhao,<sup>§</sup> Tianren Zhang,<sup>§</sup> Zhigang Zou<sup>†</sup>*

<sup>†</sup>Jiangsu Key Laboratory for Nano Technology, National Laboratory of Solid State Microstructures, College of Engineering and Applied Sciences, and Collaborative Innovation Center of Advanced Microstructures, Nanjing University, 22 Hankou Road, Nanjing 210093, China.

<sup>‡</sup>Kunshan Innovation Institute of Nanjing University, Kunshan Sunlaite New Energy Co., Ltd., Kunshan, 1699# South Zuchongzhi Road, Suzhou 215347, China.

<sup>§</sup>R & D Department, Zhejiang Tianneng Energy Technology Co., Ltd., Changxing Zhejiang 313100, China

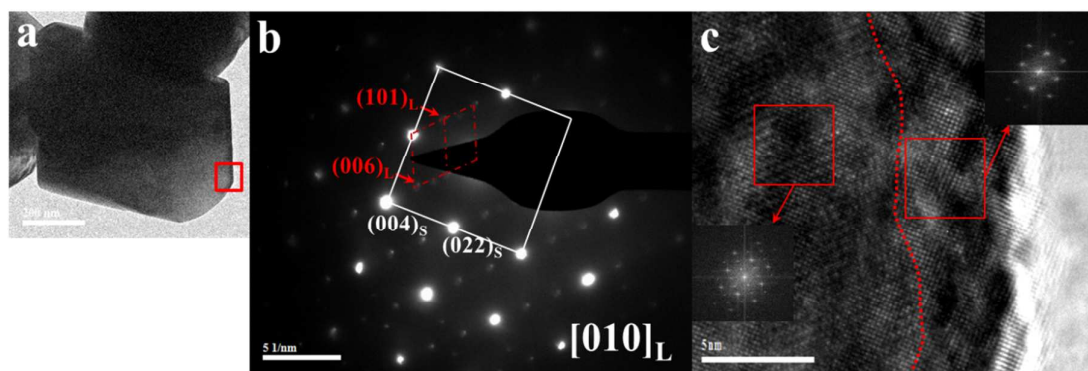
## Corresponding Author

\*E-mail: [jianguoliu@nju.edu.cn](mailto:jianguoliu@nju.edu.cn) (J. L.).

\*E-mail: [vict.sun@gmail.com](mailto:vict.sun@gmail.com) (W. S.)

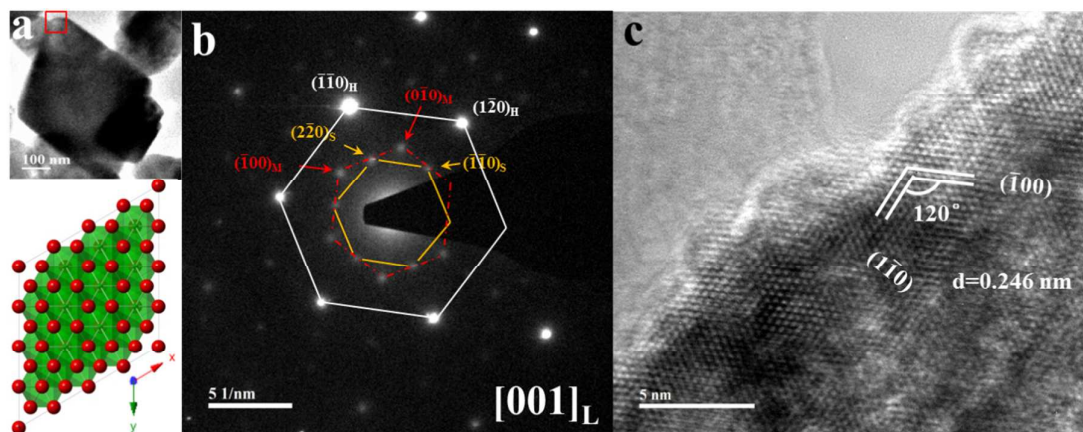
**Table S1.** ICP-OES results of precursor, C-LMNCO and CG-LMNCO samples, respectively.

Sample	Mn (%)	Ni (%)	Co (%)
Precursor	29.62	7.49	8.29
C-LMNCO	35.47	9.04	8.73
CG-LMNCO	35.35	9.25	8.23



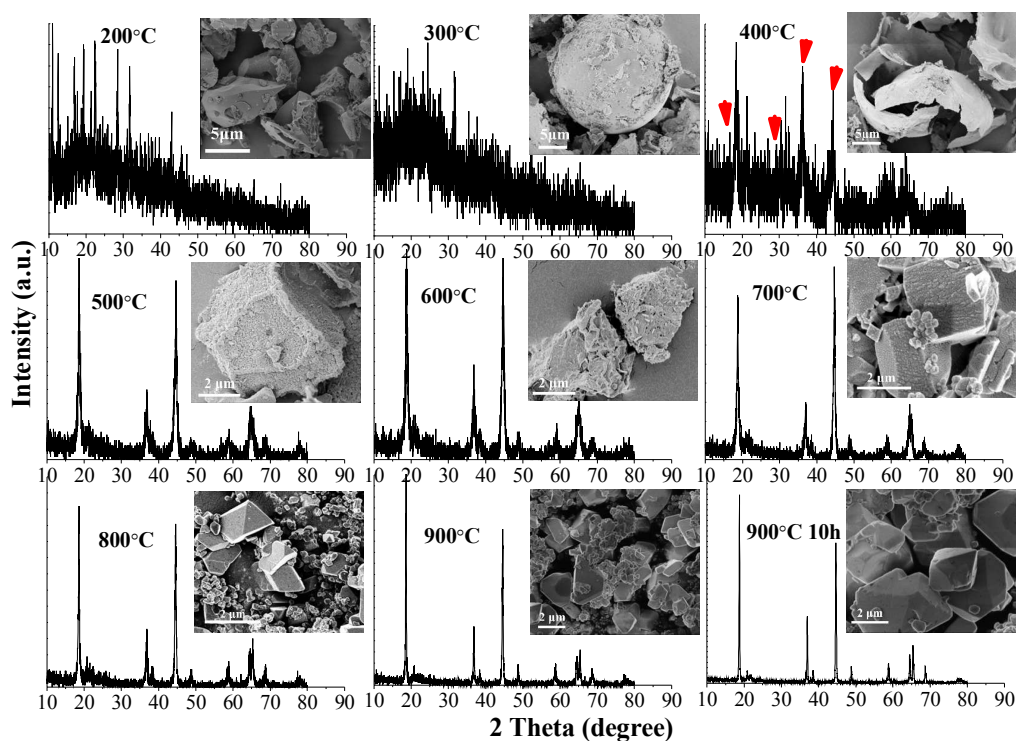
**Figure S1.** TEM image (a), SAED pattern (b) and HRTEM image (c) of CG-LMNCO along the  $[010]$  layered zone axis in another region.

Figure S1a is a low-magnification TEM view showing a representative pristine CG-LMNCO microparticle in another region, and its SAED pattern along the  $[010]_L$  zone axis shown in Figure S1b confirms the coexistence of the layered and spinel structures in CG-LMNCO crystals. Figure S1c clearly shows the presence of a spinel phase shell about 5 nm wide approximately the surface of the layered bulk structure outlined by a red dotted line according to FFT patterns from the surface region.



**Figure S2.** TEM image (a), SAED pattern (b) and HRTEM image (c) of CG-LMNCO along the [001] layered zone axis.

Figure S2 represents the electron diffraction of CG-LMNCO along the [001] layered zone axis. SAED presents (Figure S2b) clear evidence of the coexistence of  $\text{LiMO}_2$  ( $\text{M} = \text{Ni, Co, Mn}$ ),  $\text{Li}_2\text{MnO}_3$  and  $\text{Li}_x\text{Mn}_2\text{O}_4$  domains. The pattern can be considered to be the superposition of a hexagonal layered structure pattern, monoclinic structure pattern and cubic spinel structure pattern, respectively. The zone axis applied for them are  $[001]_L$  and  $[111]_S$ . The HRTEM pattern in Figure S2c represents that the frontal plane displaying two sets of lattice fringes with the same interplanar distance of 0.246 nm and an angle of  $120^\circ$  with no other orientations, because all atoms (TM, Li, O) are overlapping in the  $[001]_L/[111]_S$  directions. So it can be concluded that there is an overgrowth of the spinel structure on  $\{001\}_L$  facets of the layered structure with  $\{111\}_S$  facets, and these two phases share a similar two-fold symmetry with a  $[001]_L/[4\bar{1}\bar{1}]_S$  parallel orientation.



**Figure S3.** The XRD patterns and simultaneous SEM images of CG-LMNCO under different temperatures.

As shown in Figure S3, it can be observed that the precursors are buried in a hydrocarbon compound and divided into many pieces at 200 °C. And then CA decomposes at 300 °C with the removal of CO<sub>2</sub> and H<sub>2</sub>O, resulting in the decomposition of spherical precursors, which is carried out thoroughly and only part of residual spherical shell remains at 400 °C. Meanwhile, many impurities and a noticeable pure phase corresponding to M<sub>3</sub>O<sub>4</sub> (M = Mn, Ni and Co) (JCPDS NO. 18-0803) are generated with poor crystallinity under 400 °C based on the result of XRD patterns indicated by the red arrows. This result indicates that a tetragonal spinel phase is introduced in the early stages of synthesis under the effect of CA combined with adsorption and decomposition, with the material undergoing the reaction  $\text{MnCO}_3 + \text{O}_2 \rightarrow \text{Mn}_3\text{O}_4$  rather than  $\text{Mn}^{2+}/\text{MnCO}_3 + \text{O}_2 \rightarrow \text{MnO}_2$  for the sol-gel or general coprecipitation method. Soon, as the process gets under way, a hexagonal layered phase is formed and the identified peaks gradually grow more sharper from 500 °C to 700 °C. More

and more angular aggregations emerge instead of irregular residual spherical shells at the same time as observed by SEM. The XRD pattern shows that most of the tetragonal spinel phase disappeared because of the increased Mn oxidation. The added larger octahedral particles that are mainly composed of a layered structure become mature gradually with the increase of reaction time and temperature, along with the decrease of small and irregular ones. However, a small amount of residual spinel phase is preserved on the surface of crystals with a high percentage of exposed  $\{111\}_s$  facets because of the thermodynamic stability of spinel  $\text{Mn}_3\text{O}_4$ . Coincidentally, the burning carbon produces a large amount of heat accompanied by emission of  $\text{CO}_2$ , removing O and Li from the surface structure of particles, which generates a sufficient number of vacancies for Li and O. Mn, which should be in the octahedral sites of the TM layer migrates to octahedral sites in the Li layer to form a spinel framework on the surface of particles. On the basis of the XRD and SEM results above, the mechanism of an octahedral core-shell structure formed in layered oxide cathodes through the coprecipitation-gel method can be well explained.

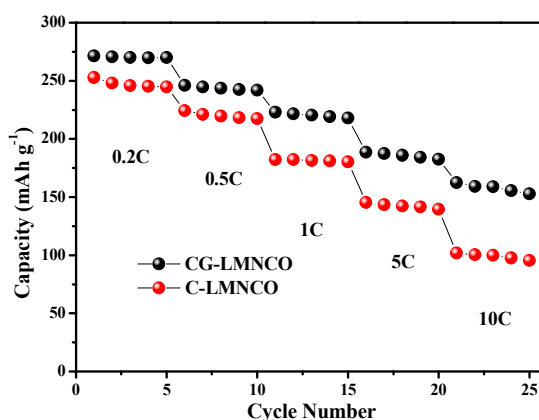


**Figure S4.** The rate performances of CG-LMNCO and C-LMNCO in the voltage range of 2.0-4.8 V.

The rate capabilities of C-LMNCO and CG-LMNCO samples discharged at different rates are illustrated in Figure S4. For the two samples, the discharge capacity decreases with

increasing discharge rate, indicating that electrochemical polarization exists. However, CG-LMNCO sample exhibits a higher rate capability than for the C-LMNCO sample. Particularly, CG-LMNCO sample with the best rate of discharge performance presents a discharge capacity of 271.2 mAh g<sup>-1</sup>, 245.9 mAh g<sup>-1</sup>, 222.9 mAh g<sup>-1</sup>, 188.5 mAh g<sup>-1</sup>, and 162.4 mAh g<sup>-1</sup> at 0.2 C, 0.5 C, 1C, 5 C, and 10 C, respectively. For comparison, the discharge capacities of C-LMNCO sample were 252.7 mAh g<sup>-1</sup>, 224.1 mAh g<sup>-1</sup>, 182.1 mAh g<sup>-1</sup>, 145.2 mAh g<sup>-1</sup>, and 101.8 mAh g<sup>-1</sup> under the same conditions.

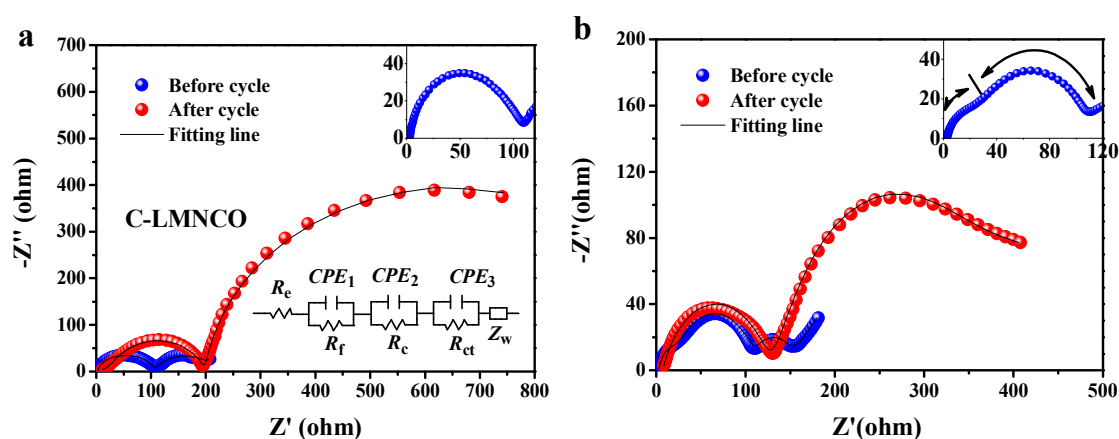


**Figure S5.** Nyquist plots of C-LMNCO (a) and CG-LMNCO (b) electrodes before and after 100 cycles in the range 2.5~4.4 V at 0.5 C, respectively.

**Table S2.** Electrode impedance parameters obtained from the equivalent circuit fitting of experimental data for C-LMNCO and CG-LMNCO.

Sample	Condition	$R_e$ [ $\Omega$ ]	$R_f$ [ $\Omega$ ]	$R_c$ [ $\Omega$ ]	$R_{ct}$ [ $\Omega$ ]
C-LMNCO	Before	2.89	40.35	62.59	104.6
	100 th	3.27	38.75	156.9	912
CG-LMNCO	Before	3.08	18.18	87.94	34.71

100 th	7.24	13.5	110.8	311.8
--------	------	------	-------	-------

---

EIS was applied to study the kinetic properties of C-LMNCO and CG-LMNCO samples before and after the 100th cycle in the range 2.5~4.4 V at 0.5 C cycles. Before EIS measurements, both samples after the 100th cycle were charged to 3.8 V to reach an identical status, and the results are shown in Figure S5a and b, respectively. The inset in Figure S5a is an equivalent electrical circuit for analyzing impedance spectra, and corresponding fitting data are given in Table S2. As shown in Figure S5a and b, the fitting results and experimental data match very well. The spectra of pristine C-LMNCO consists of a semicircle in the high frequency, a larger semicircle in the middle frequency region and a straight line with about a 45° angle in the low frequencies. These are attributed to the impedance ( $R_f$ ) of  $\text{Li}^+$  diffusion through the surface layer on cathode particles, the impedance of charge transfer reaction ( $R_{ct}$ ) and Warburg impedance of the solid-state diffusion of Li ions through the bulk structure of the electrode ( $Z_w$ ), respectively. But for pristine CG-LMNCO, the Nyquist plot clearly contains four identifiable separated parts, essentially three semicircles and one line. As can be seen from the top right corner of Figure S5b, the Nyquist plots of the pristine CG-LMNCO sample show a unique depressed small semicircle between from middle to high frequency range. The phenomenon has never been reported before in the literature of Li-rich layered materials. According to the research of Nobili<sup>1-2</sup> and Sun *et al.*,<sup>3</sup> this second semicircle is related to the electronic properties of the material.  $\text{LiMO}_2$  (M = Mn, Ni and Co) materials are a *p*-type semiconductor which conducts by insulator-to-metal transition during the deintercalation process.<sup>4-5</sup> Sufficient electron holes are created within the valence band accompanied by enough Li deintercalation from the  $\text{LiMO}_2$  lattice. And  $\text{LiMO}_2$  exhibits metallic-like electronic properties in this regime. This further proves that more Li vacancies



in the CG-LMNCO sample are created at the electrode/electrolyte interface compared to C-LMNCO samples, as supported by the results above. More interestingly, the first semicircle in the high frequency and the second semicircle between the middle to high frequency range of CG-LMNCO overlapped each other and were merged into one single compressed semicircle after 100 cycles, which can be attributed to Li ions recapturing the electron holes. The higher values of  $R_f$  and  $R_c$  indicate a difficult migration of Li ions through the surface layer on cathode particles for C-LMNCO electrodes. This proves that a rock-salt phase has been generated in the surface and formed a relatively nonreactive layer. In addition, the  $R_{ct}$  of C-LMNCO, 912.0  $\Omega$ , is also much larger than that of CG-LMNCO, 311.8  $\Omega$ . This indicates reduced polarization and quicker transfer of Li ions on the electrode/electrolyte interface for the CG-LMNCO sample.

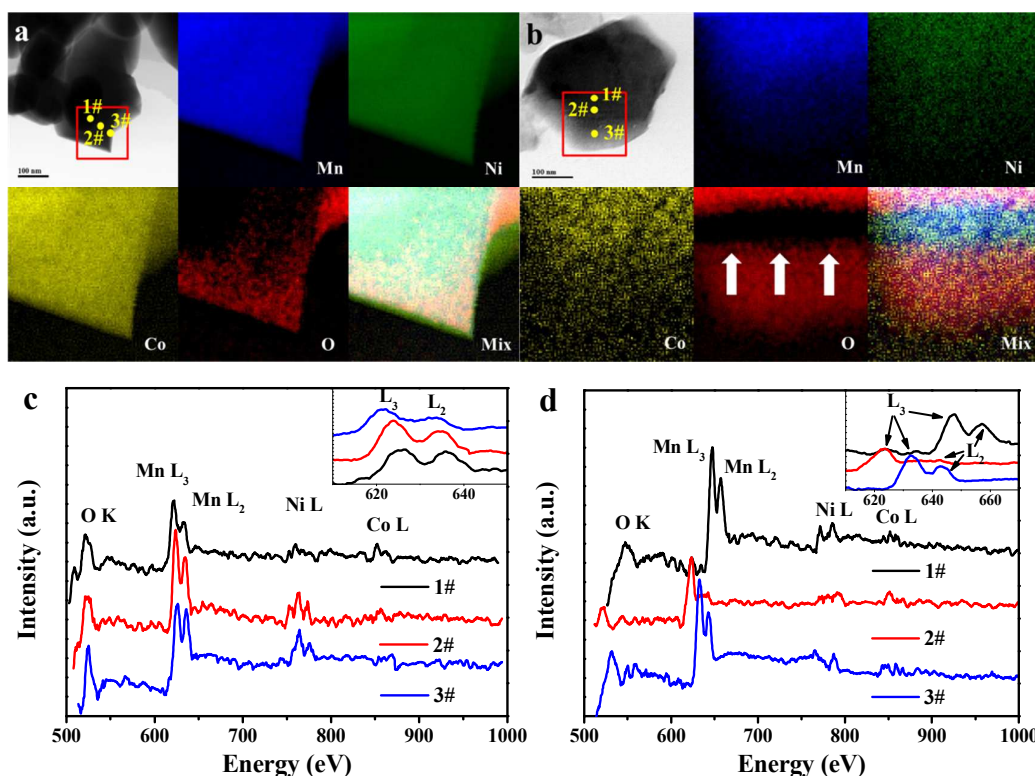


**Figure S6.** EELS mapping images of C-LMNCO (a) and CG-LMNCO (b), EELS spectra obtained from the surface to the bulk structure of C-LMNCO (c) and CG-LMNCO (d) after



20 cycles.

Figures S6a and b present EELS mapping of the local region of the C-LMNCO and CG-LMNCO parts after 20 cycles in the range of 2.0~4.8 V at 0.1 C, respectively (represented by the red boxes in Figures S6a and b, respectively). According to the oxygen map, expansive oxygen-deficient areas can be observed in the bulk domains for the both samples, while the other elements' contents distribute uniformly in the entire region. Similarly, the O map of the CG-LMNCO sample in Figure S6b shows an expanded dark belt, which indicates a sustained decrease of O concentration within this region during electrochemical cycling. As shown in Figure S6c and d, the O K edge profiles and Mn L<sub>3</sub> and L<sub>2</sub> profiles of C-LMNCO shift to a lower-energy region at the oxygen-deficient regions (marked with yellow dots in Figure S6a and b). These results further prove the outward diffusion mechanism that O anions travel from the bulk structure to the surface region. The oxygen loss at surface regions is replenished from the bulk region, which accordingly results in a lower oxygen concentration in the bulk structure while relatively maintaining the oxygen content in the surface regions.

## REFERENCES

- (1) Nobili, F.; Tossici, R.; Marassi, R.; Croce, F.; Scrosati, B., An AC Impedance Spectroscopic Study of Li<sub>x</sub>CoO<sub>2</sub> at Different Temperatures. *J. Phys. Chem. B* **2002**, *106*, 3909-3915.
- (2) Nobili, F.; Dsoke, S.; Croce, F.; Marassi, R., An AC Impedance Spectroscopic Study of Mg-doped LiCoO<sub>2</sub> at Different Temperatures: Electronic and Ionic Transport Properties. *Electrochim. Acta* **2005**, *50*, 2307-2313.

- (3) Zhuang, Q.-C.; Wei, T.; Du, L.-L.; Cui, Y.-L.; Fang, L.; Sun, S.-G., An Electrochemical Impedance Spectroscopic Study of the Electronic and Ionic Transport Properties of Spinel  $\text{LiMn}_2\text{O}_4$ . *J. Phys. Chem. C* **2010**, *114*, 8614–8621.
- (4) Qiu, X.-Y.; Zhuang, Q.-C.; Zhang, Q.-Q.; Cao, R.; Ying, P.-Z.; Qiang, Y.-H.; Sun, S.-G., Electrochemical and Electronic Properties of  $\text{LiCoO}_2$  Cathode Investigated by Galvanostatic Cycling and EIS. *Phys. Chem. Chem. Phys.* **2012**, *14*, 2617-2630.
- (5) Qiu, X.-Y.; Zhuang, Q.-C.; Zhang, Q.-Q.; Cao, R.; Qiang, Y.-H.; Ying, P.-Z.; Sun, S.-G., Investigation of Layered  $\text{LiNi}_{1/3}\text{Co}_{1/3}\text{Mn}_{1/3}\text{O}_2$  Cathode of Lithium Ion Battery by Electrochemical Impedance Spectroscopy. *J. Electroanal. Chem.* **2012**, *687*, 35-44.